In-situ Oxidation Study of Pt Nanoparticles on MgO(001)

Uta Hejral,[†,‡,¶] Alina Vlad,[†,§] Philipp Nolte,[†] and Andreas Stierle[*,†,‡,¶]

Max-Planck-Institut für Intelligente Systeme (former Max-Planck-Institut für Metallforschung), Heisenbergstr. 3, 70569 Stuttgart, Germany, and Fachbereich Physik Universität Hamburg, Jungiusstr. 9, 20355 Hamburg, Germany

E-mail: andreas.stierle@desy.de

*

Abstract

Noble metal nanoparticles supported by oxide carriers are widely employed in heterogeneous catalysis. In order to improve catalyst efficiency it is important to understand oxidation processes on the atomic scale. Here we studied oxygen-induced shape changes of Pt nanoparticles on MgO(001) by means of in-situ surface x-ray diffraction (SXRD) and x-ray reflectivity measurements (XRR). The x-ray results on the particle morphology were complemented by transmission electron microscopy (TEM) studies. The samples were prepared by means of physical vapor deposition and differed in average particle size and lateral particle size distribution. The oxygen-induced particle shape changes were found to be independent of particle size

[*]To whom correspondence should be addressed

[†]Max-Planck-Institut für Intelligente Systeme (former Max-Planck-Institut für Metallforschung), Heisenbergstr. 3, 70569 Stuttgart, Germany

[‡]Fachbereich Physik Universität Hamburg, Jungiusstr. 9, 20355 Hamburg, Germany

[¶]Deutsches Elektronen-Synchrotron DESY, Notkestr. 85, 22607 Hamburg, Germany

[§]Synchrotron SOLEIL, Saint Aubin BP 48, 91192 Gif-sur-Yvette Cedex, France

[*]tel: ++49 (0)40 8998 2005

and were characterized by the emergence of higher indexed facets. We propose a particle size-dependent oxidation behavior with a kinetically hindered bulk oxide formation. The formed bulk oxide structures were concluded to be (110)-oriented Pt_3O_4 and a modified structure of (0001)-oriented α-PtO_2. CO exposure of the oxidized particles did not lead to a shape change reversibility.

Keywords

Model Catalyst, Particle Shape Changes, Carbon Monoxide, Platinum Bulk Oxides.

Introduction

Pt nanoparticles dispersed on oxide carrier materials are widely used as heterogeneous catalysts with applications ranging from hydrocarbon and CO oxidation catalysis in exhaust converters to the production of fine chemicals [1,2]. Moreover, they are the most effective element employed in proton exchange membrane (PEM) fuel cells [3–10].

In order to optimize catalyst activity, selectivity and lifetime it is inevitable to understand chemical reactions and oxidation processes on the atomic scale and under realistic pressure and temperature conditions [2,11–13]. This includes understanding the formation, structure and morphology of surface oxides on various particle facets and of bulk oxides at a later oxidation stage. It is necessary to track oxygen-induced nanoparticle shape changes since the exposure of new particle facets may lead to totally different physical particle properties [2,14–17]. In addition the CO oxidation mechanism over 4d and 5d transiton metal surfaces and nanoparticles is a topic of current discussion [18–27].

Single crystal surfaces such as Pt(111), Pt(100) and Pt(110) or higher indexed facets can be seen as model surfaces for nanoparticle facets for which initial oxygen adsorption and oxide formation have been extensively studied [28–50]:

For the Pt(111) surface an ultrathin α-PtO_2 layer consisting of two O-Pt-O trilayers was observed

as thickest oxide film forming under harsh oxidation conditions of 0.5 bar O_2 pressure at 770 K: in-situ surface x-ray diffration (SXRD) disclosed that it grows in a hexagon-on-hexagon arrangement leading to a (8×8) coincidence superstructure unit cell [34]. In a recent study employing in-situ x-ray photoeletron spectroscopy (XPS), x-ray absorption spectroscopy (XAS) and DFT simulations the precursor to this trilayer oxide was proposed to be a PtO-like surface oxide coexisting with chemisorbed oxygen [35]. The bulk oxide structure on the Pt(111) surface was found to consist of thermally stable three-dimensional clusters of α-PtO_2 which are expected to be less reactive toward CO oxidation than lower coverage oxygen phases [36,41].

For oxygen coverages higher than 1 ML the growth of α-PtO_2 oxide particles - preceded by a precursor state - was concluded to be promoted on the Pt(100) surface [41,42]. This finding is in accordance with DFT calculations which propose the possibility of a α-PtO_2 trilayer to emanate from a p(2×1) structure and to form on the Pt(100) surface [15]. However, also Pt_3O_4 bulk oxide formation originating from a PtO-like structure was suggested [40].

On the Pt(110) surface oxygen exposure leads at a later oxidation stage to a phase consisting of (12×2) stripes oriented along the $\langle 1\bar{1}0 \rangle$ direction which progressingly dominates with increasing temperature [46–48]. According to DFT calculations α-PtO_2 represents a stable bulk oxide structure [15,47]. Recent studies in which AP-XPS, HP-STM and DFT calculations were combined propose at elevated O_2-pressures of 0.5 Torr the coexistence of α-PtO_2 domains of at least two layers thickness along with regions of metallic Pt with chemisorbed oxygen [25]. These results are in accordance with STM and SXRD measurements performed in a gas flow reactor [24]: a distorted incommensurate α-PtO_2 film and a commensurate (1×2) oxide layer were deduced, where the latter occured to be the more active structure for CO oxidation and only stable when both O_2 and CO were present at sufficiently high temperatures.

Based on the Wulff construction [51] and on DFT calculations the thermodynamically stable equilibrium Pt particle shape in dependence of the oxygen chemical potential μ(p,T) was determined taking into account the stability of the various oxygen adsorption structures and surface oxides [15]. These findings based on results obtained for the oxidation of single crystal surfaces, however, can-

not simply be assigned to the equivalent nanoparticle facets: the presence of vicinal surfaces and edges, the higher defect density and the influence of the substrate which are present in nanoparticle systems may lead to a different oxidation behavior which in turn might also affect catalyst performance [13,52,53]. This underlines the explicit need for experimental in-situ studies of oxygen-induced nanoparticle shape changes and bulk oxide formation under realistic conditions.

Not much is known about the structure of completely oxidized Pt nanoparticles either. In a recent study combining atomic force microscopy (AFM), transmission electron microscopy (TEM), XPS and thermal programmed desorption (TPD) the size dependence of Pt nanoparticles with respect to bulk oxide formation and the thermal stability of the resulting Pt oxides was investigated [54]. It was concluded that oxide formation was more favorable on smaller particles. By means of XPS the formed bulk oxide structures were identified as α-PtO_2 (or Pt_3O_4) and PtO. The TPD measurements disclosed higher O_2 desorption temperatures for Pt nanopaticles than for a Pt(111) surface. However, since in XPS spectra the peaks of various Pt bulk oxides (PtO, α-PtO_2, Pt_3O_4) can be found at similar energies it is very difficult to retrieve the true bulk oxide structures [54–56]. To our knowledge studies revealing detailed information about the structure of oxidized epitaxial Pt nanoparticles and the spatial orientations of their oxides with respect to the substrate are missing so far but would be of utmost importance for an improved understanding of the oxidation process on an atomic scale.

In this work we present our results on oxygen-induced size and shape changes of Pt nanoparticles on an oxide support (MgO(001)) for temperatures between 493 K and 673 K and oxygen pressures ranging from UHV up to 500 mbar. The results were obtained by in-situ grazing incidence x-ray diffraction (GIXRD), x-ray reflectometry (XRR) and complementary TEM measurements. In the experimental section the sample preparation as well as our approach to study and analyze particle size and shape changes will be outlined. We will present our results on the structure and morphology of the nanoparticles under UHV conditions. This includes information about particle size, shape and the epitaxial relationship of the particles with respect to the substrate. Since the two samples presented here were prepared under different conditions their morphological differ-

ences will be pointed out. Subsequently, we will present the particle size and shape changes that occured during in-situ oxidation at 573 K and 493 K, respectively. Furthermore, the structure of the bulk oxides that had formed during oxidation at a slightly higher temperature of 673 K will be discussed. The results section will close with our findings on the CO exposure of the oxidized particles.

Experimental

Apart from the cube-on-cube epitaxy - referred to as $[100](001)_{Pt} \parallel [100](001)_{MgO}$ - two types of (111)-orientations - denoted by $[1\bar{1}0](111)_{Pt} \parallel [110](001)_{MgO}$ and $[1\bar{1}0](111)_{Pt} \parallel [100](001)_{MgO}$ - have been observed so far for the growth of Pt particles on MgO(001) [57–65]. Here we make use of the same notation for the different particle epitaxies as employed in [57]. In the framework of our study we aimed at growing particles with cube-on-cube epitaxy since their particle shape can easily be deduced by mapping crystal truncation rod signals from particle facets in reciprocal space [14]. The comparison between maps measured under UHV and oxidizing conditions yields the particle shape changes that occur during in-situ oxidation.

The first step in the sample preparation comprised the annealing of the empty MgO(001) substrates (10 mm $\times$ 10 mm $\times$ 1 mm with a miscut smaller than 0.1 $^\circ$) in air at 1273 K in a tube furnace for one hour where a heating and cooling rate of 20 K/min was used. Since annealing results in surface segregation of bulk impurities (mainly of Ca) the samples underwent thereafter repeated cycles of Ar^+ sputtering (U=600 V) and of annealing at 773 K under 10^{-5} mbar oxygen pressure in a stationary UHV chamber. The cleanliness of the surface was afterwards confirmed by Auger electron spectroscopy (AES).

For the subsequent physical vapor deposition of Pt a substrate temperature of 973 K was used since it was in previous studies found to result in particles favoring cube-on-cube epitaxy [57]. In case of sample I the sample heating was switched off directly after Pt deposition whereas sample II underwent further annealing at 1073 K for $\sim$30 more minutes. Prior to the synchrotron x-ray

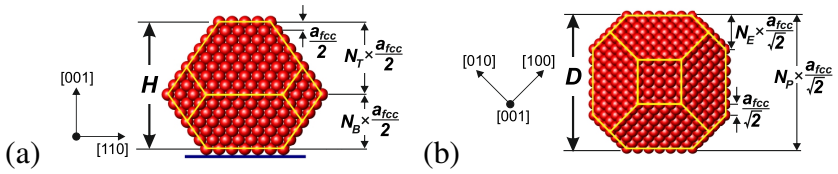

Fig. 1: Parameters N_P, N_E, N_T and N_B that constitute the quantitative particle shape: (a): the particle height is calculated using $H = \frac{(N_T+N_B)\cdot a_{fcc}}{2}$, (b): the particle diameter via $D = \frac{N_P \cdot a_{fcc}}{\sqrt{2}}$.

investigations sample I had been in air whereas sample II had permanently been kept under UHV conditions.

The samples were investigated at the MPI-MF beamline at the ANKA synchrotron (ANgströmquelle KArlsruhe) at a photon energy of 10 keV using a point detector for reciprocal space mapping [66]. The in-situ oxidation studies were carried out in a mobile UHV chamber suited for high pressure studies. It is equipped with a gasline system for well-defined gas introduction and three pressure gauges - each appropriate for a different pressure region - allow to measure pressures ranging from UHV to 1.3 bars. The chamber includes a high pressure compatible filament heating station which reaches temperatures up to 923 K with an accuracy of $\pm$20 K. Based on a calibration curve the temperature was controlled via its filament current. The incident angle of the beam was kept fixed at α_{in} = 0.22 $^\circ$ and thus slightly below the critical angle of MgO ($\alpha_{c,MgO}$ = 0.221 $^\circ$) in order to suppress bulk scattering and to enhance surface sensitivity.

For the quantitative analysis of the UHV particle shape and the oxygen-induced particle size changes of sample I two approved procedures were combined [14,67]. Both assume as underlying model for the particle shape under UHV conditions a truncated octahedron according to the Wulff-Kashiew construction. As displayed in Fig. 1(a) this shape can be expressed by means of the four parameters N_P, N_E, N_T and N_B.

In the first procedure the FWHMs (full width at half maximum) of scans through Pt particle Bragg peaks along high symmetry directions were calculated in dependence of the particle parameters and compared to the corresponding FWHMs obtained experimentally. In this way the average particle height and diameter of sample I under UHV and oxidizing conditions were obtained.

In the second procedure reciprocal space maps along directions containing particle facet signals were simulated in dependence of the particle parameters of Fig. 1. Fitting the simulated maps to the experimentally obtained ones by varying the background and a scaling factor resulted in the quantitative particle shape.

In the data analysis the size distribution of the particles was taken into account since it has an impact on the FWHM of the particle Bragg peaks. The size distribution was obtained by the analysis of various TEM plain view images two of which are shown in Fig. 3(a) and (b). For both samples the TEM plain view and cross section images were measured after the corresponding beamtimes and the successive in-situ oxidation cycles performed within. Aiming at the removal of possible formed oxides sample I had been annealed at 973 K for ∼80 minutes, sample II at 923 K for ∼40 minutes prior to the TEM measurements. For the TEM measurements slices of the sample were sandwiched face to face employing epoxy. After that the sandwiched sample was sliced along the $\langle 110 \rangle_{MgO}$ direction and ion-milled until perforation [68]. The measurements were carried out using a JEOL 4000 FX microscope and a GATAN Orius 200 C CCD camera at an electron acceleration of 400 kV. High resolution images in cross section view were performed in dark imaging mode whereas bright field imaging was used for measuring plain view images.

Results

Particle Structure and Morphology Prior to Oxidation

The top and centre curve in Fig. 2(a) show specular x-ray reflectivity (XRR) data measured on the two samples under UHV conditions at 573 K in case of sample I and 493 K in case of sample II. Sample I had before been exposed to $4.2 \cdot 10^{-1}$ mbar O_2 pressure and had afterwards been annealed under $1 \cdot 10^{-5}$ mbar O_2 for ∼50 minutes at 873 K. Sample II had prior to the reflectivity measurements been annealed under UHV at 873 K for ∼25 minutes. As a comparison to these reflectivity data measured on MgO(001)-supported particles the solid curve at the bottom of Fig. 2(a) represents a reflectivity curve simulated for the case of an empty MgO(001) substrate. For

the simulation a similar surface roughness (σ_{MgO}=11.37 $\AA$) as present on sample I and II after Pt deposition was used.

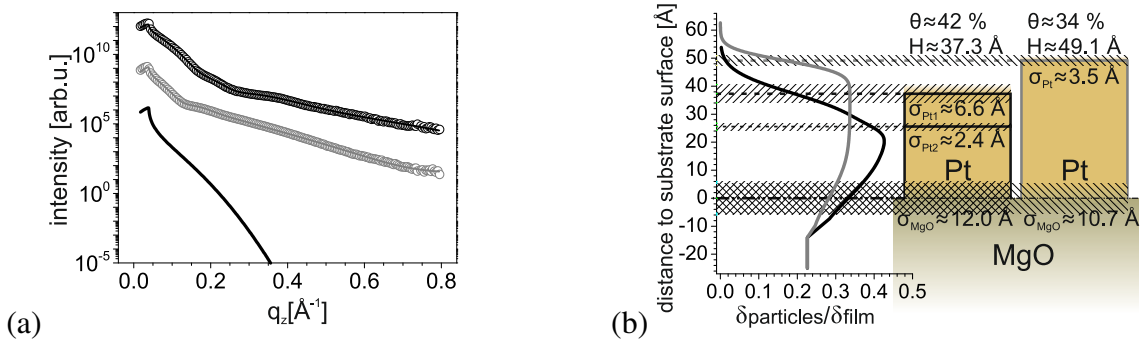

Fig. 2: Results of specular reflectivity measurements: (a): measured data are depicted as open circles, data fits as solid lines. Top curve: sample I; central curve: sample II; bottom curve: reflectivity curve simulated for the case of a bare MgO(001) substrate (σ_{MgO}=11.37 $\AA$). (b): left: electron density profiles resulting from the fits; right: underlying fit models and obtained fit parameters; hatched areas represent the corresponding interface roughnesses.

The data fits are based on simple box models in which the particles are represented by closed Pt layers (Fig. 2 (b)). The fitting procedure uses a modified Parratt formalism in which the layer roughnesses are taken into account as Gaussian-shaped fluctuations around the layer interfaces. Comparing the fitted electron density with the density literature value of bulk Pt yields the percental coverage of the particles. In case of sample I it amounts to 42 %, in case of sample II to 34 %. The particle heights were found to comprise 37 $\AA$ and 49 $\AA$ for sample I and sample II, respectively. The on average higher particles on sample II can be explained by particle sintering during the annealing process directly after Pt deposition. As explained in the supporting material the use of the box model leads to a general underestimation of the fit parameter for the particle height.

The analysis of TEM plain view images (Fig. 3) yielded similar results for the percental particle coverage: 41 % in case of sample I and 40 % in case of sample II. Furthermore, the horizontal size distribution of the particles was concluded to comprise 57 % and 83 % for sample I and II, respectively.

The epitaxial relationship of the particles with respect to the substrate was obtained by per-

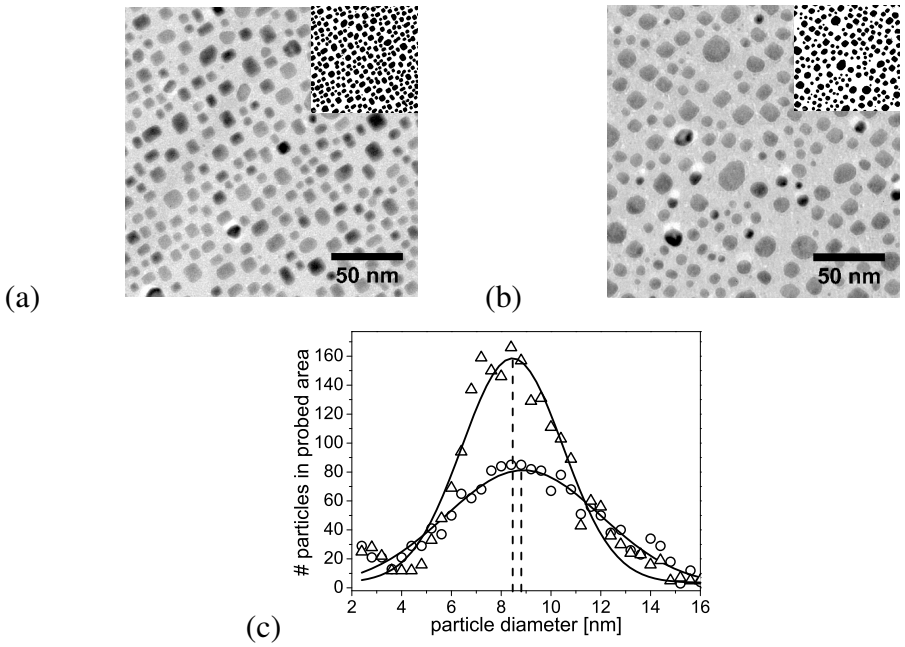

Fig. 3: Examples of TEM plain view images measured on sample I (a) and sample II (b). The insets show binary images [69] used for analyzing the horizontal size distribution of the particles. (c): number of particles in dependence of the particle diameter found for sample I (△) and sample II (○); in order to obtain the size distribution the data was fitted with Gaussians (solid lines).

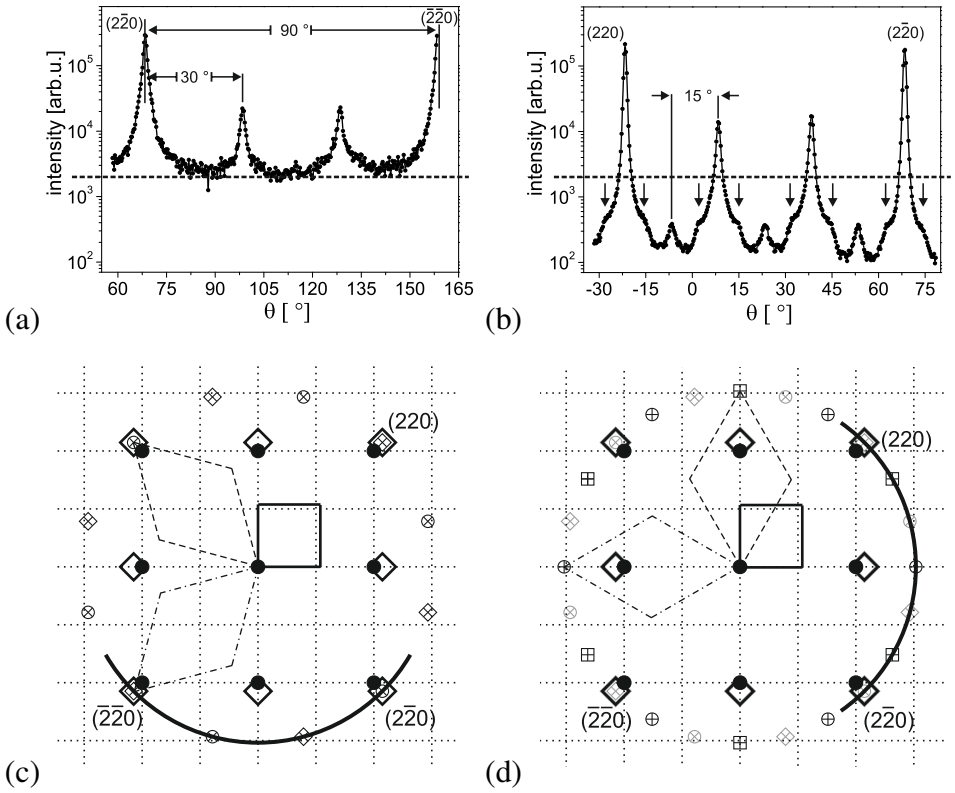

Fig. 4: Rocking scans through (220)-type Pt Bragg peaks performed on sample II, (a): on the as-prepared particles at 493 K: Bragg peaks belonging to particles with $([100](001)_{Pt}$ || $[100](001)_{MgO})$- and $([1\bar{1}0](111)_{Pt}$ || $[110](001)_{MgO})$-type epitaxies can be seen; (b): after annealing at 873 K for 25 minutes: additional peaks separated by 15 ° belonging to the $([1\bar{1}0](111)_{Pt}$ || $[100](001)_{MgO})$ epitaxy and shoulders (indicated by arrows) on the other peaks appeared. (c): in-plane reciprocal space map of Pt Bragg peak positions found in the scan displayed in (a): $\diamondsuit$: Bragg peaks of the $([100](001)_{Pt}$ || $[100](001)_{MgO})$ epitaxy; $\diamondsuit\!\!\!\!\otimes$, $\otimes$: Bragg peaks of two domains of the $([1\bar{1}0](111)_{Pt}$ || $[110](001)_{MgO})$ epitaxy; ●: MgO Bragg peaks. (d): in-plane reciprocal space map of Pt Bragg peak positions found in the scan displayed in (b): black symbols: Bragg peak positions of two domains of the $([1\bar{1}0](111)_{Pt}$ || $[100](001)_{MgO})$ epitaxy that occurred after annealing; grey symbols: Bragg peaks of the $([1\bar{1}0](111)_{Pt}$ || $[110](001)_{MgO})$ epitaxy already present in (c) are indicated by grey symbols. The scans of (a) and (b) are represented by solid circles; straight dashed, dash-dotted and solid lines indicate unit cells of the discussed particle epitaxies.

forming rocking scans through Pt particle Bragg peaks (see Fig. 4). The rocking scan of Fig. 4(a) displays (220)-type peaks that are 90 ° apart and highest in intensity. They belong to particles growing with cube-on-cube epitaxy. Peaks of (111)-oriented particles appear every 30 ° and belong to two domains of the $[1\bar{1}0](111)_{Pt}$ || $[110](001)_{MgO}$ epitaxy. Fig. 4(c) indicates the scan position of Fig. 4(a) with respect to the Bragg peaks of the cube-on-cube and (111)-type epitaxies. According to integrated intensities the particles growing with (111)-orientation comprise only 15 % whereas the particles growing in cube-on-cube epitaxy constitute 85 % and are thus clearly predominant. Peaks of the other (111)-type epitaxy - denoted by $[1\bar{1}0](111)_{Pt}$ || $[100](001)_{MgO}$ - were clearly not present under these conditions. The high background in the scan of Fig. 4(a) implies a relatively high fraction of disordered polycrystalline Pt present on the sample surface.

Fig. 4(b) shows the same type of scan performed after the sample had been annealed at 873 K for ∼25 minutes. The annealing led to the emergence of additional peaks belonging to the $[1\bar{1}0](111)_{Pt}$ || $[100](001)_{MgO}$-type epitaxy as well as to shoulders on the Bragg peaks of higher intensity. Fig. 4(d) displays the position of the scan of Fig. 4(b) with respect to in-plane Bragg peak positions belonging to two domains of the old (grey symbols) and the new (black symbols) (111)-epitaxy which emerged after annealing. Compared to the scan of Fig. 4(a) the background had strongly decreased.

We propose that annealing led to ordering of the powder and to formation of particles growing with $[1\bar{1}0](111)_{Pt}$ || $[110](001)_{MgO}$-type epitaxy as well as to particles which are misoriented with respect to the main epitaxies and which hence give rise to the peak shoulders. After annealing particles with cube-on-cube epitaxy are still predominant and comprise 85 %, where the shoulders were included in the integration. Particles belonging to the $[1\bar{1}0](111)_{Pt}$ || $[110](001)_{MgO}$ epitaxy constitute 13 %, particles belonging to the $[1\bar{1}0](111)_{Pt}$ || $[110](001)_{MgO}$ epitaxy amount to 2 %. Shoulder intensities on the larger peaks deviate up to 10-11 ° from the peak maxima. These findings are in accordance with a combined experimental and theoretical study which proposes that for clusters with a diameter smaller than 2 nm not only the $[1\bar{1}0](111)_{Pt}$ || $[110](001)_{MgO}$-type epitaxy is favorable but also misorientation angles up to 15 ° [57]. The most stable misorientations

were calculated to appear up to 11 ° of deviation [57]. Thus, we assume that the newly formed particles are of a rather small size. In line with this assumption are our TEM plain view measurements on sample II which - contrary to measurements performed on sample I - revealed a large lateral particle size distribution and the presence of a multitude of smaller particles.

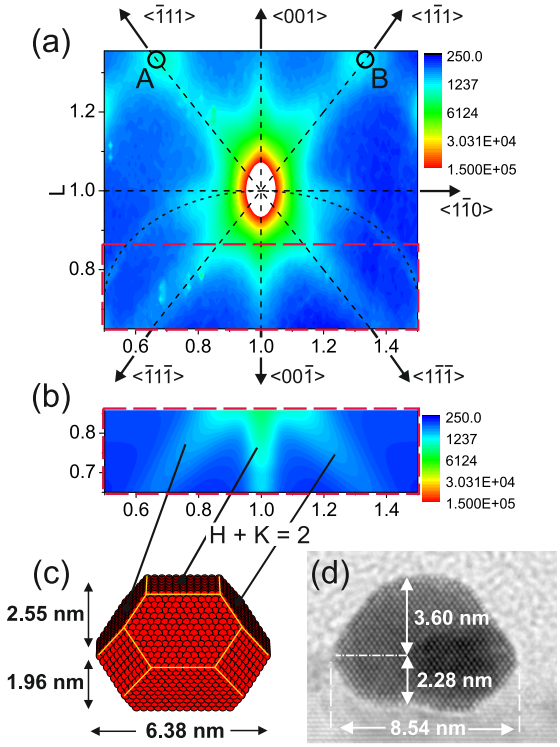

Fig. 5: (a): Experimentally obtained reciprocal space map of sample I measured under UHV conditions in the (H+K=2)-plane at 573 K; dashed lines indicate the calculated positions for (001)- and (111)-type facets signals, the peaks labeled A and B stem from internal twinning, the dashed circle indicates the intensity caused by particles tilte with respect to the surface normal. (b): corresponding fit of the lower part of the map (dashed box) from which the parameters N_P=23, N_E=7, N_T=13 and N_B=9 were deduced. (c): quantitative particle shape obtained from the fit. (d): TEM cross section view of a particle on sample I measured after the in-situ oxidation studies and annealing.

According to our quantitative Bragg peak analysis (see online supporting material) the particle diameter and height of sample I under UHV conditions at 573 K were concluded to amount to H=47±10 *Å* and D=64±6 *Å*. The FWHM of the Bragg peaks in case of sample II yield at 493 K and under UHVconditions a particle height and diameter of H=58±4 *Å* and D=112±8 *Å*.

Reciprocal space mapping was used to obtain the quantitative particle shape under UHV conditions. Fig. 5(a) shows the reciprocal space map in the (H+K=2, L)-plane measured on sample I. It is centered around the Pt(111) Bragg peak and displays crystal truncation rod signals from (001)-, (111)- and (110)-type particle facets. The strong intensity of the (111)- and (001)-type signals indicates that these facets dominate the particle shape under these conditions as expected from the Wulff-construction. The ring-like smearing out of the Pt(111) Bragg peak signal is caused by particles that are tilted with respect to the surface normal. The location of this additional intensity is indicated by the dashed circle segment in Fig. 5(a) and overlaps with possible signal of (110)-type side facets. Maps measured in the horizontal reciprocal space plane confirmed the existence of both (110)-type and (100)-type side facets. The areas with higher intensities labeled A and B stem from internal twinning. Comparing their signal intensity to the Bragg peak intensity yields the percentage of planes with inverted stacking compared to regular planes which amounts to only 0.15 %.

For the quantitative particle shape analysis the lower part of the experimental map (Fig. 5(b)) was simulated for a large number of parameter sets (N_P, N_E, N_T, N_B), where - based on the results of the quantitative Bragg peak analysis - the parameter N_P was only varied in the small range of N_P=23$\pm$2, see online supporting material. The simulated maps were fitted to the experimental ones by varying a background signal and a scaling factor. From the fit results and the comparison to the TEM cross section images the particle parameters N_P=23, N_E=7, N_T=13 and N_B=9 were obtained (see supporting material), the corresponding particle shape is shown in Fig. 5(c).This corresponds to an average particle height of H=43$\pm$4 $\mathring{A}$ which is in good accordance with the Bragg peak analysis results. Moreover, the adhesion energy of the MgO(001)-supported particles was estimated to $E_{adh} = \gamma_{100} \cdot \frac{N_T - N_B}{N_T} = 26.1 \ \frac{meV}{\mathring{A}^2}$, which is significantly lower than for Rh on MgO(100) (108 $\frac{meV}{\mathring{A}^2}$) [14]. Here $\gamma_{100} = 0.113 \ \frac{eV}{\mathring{A}}$ denotes the surface energy of the unreconstructed Pt(001) surface as calculated in [15]. Fig. 5(d) shows a TEM cross section image of a particle of sample I recorded after the in-situ oxidation studies (see next section) and additional annealing.

Oxygen-Induced Structure and Shape Changes

In the previous section we reported on the particle structure and morphology under UHV conditions. Here, we discuss the particle size and shape changes that occured when changing to oxidizing conditions. The in-situ oxidation was in case of both samples carried out by means of a stepwise controlled increase of oxygen pressure. Meanwhile linescans in the (H+K=2, L)-plane at constant L-values sensitive to particle facet signals (sample I: L=0.78; sample II: L=0.83) were performed. This allowed the immediate observation of possible intensity changes in the particle facet signals which would directly point to a change in the particle shape.

For sample I shape changes were found to set in at a temperature of 573 K and an oxygen pressure of $4.0 \cdot 10^{-3}$ mbar (μ=-0.92 eV). Fig. 6(a) shows the reciprocal space map measured at this temperature and oxygen pressure range. In Fig. 6(c) linescans sensitive to particle facet signals are shown that were extracted from the map of Fig. 6(a) (oxidizing conditions) and the map of Fig. 5(a) (UHV conditions). The linescans in Fig. 6(c) reveal an intensity increase in the region between the (111)- and (001)-type facets when changing to oxidizing conditions which can be traced back to the emergence of higher indexed facets. Their formation can also be retrieved from the difference map displayed in Fig. 6(b) which gives an overview of the global intensity changes. The intensity increase could not be ascribed to any specific type of facets so we assume the emergence of various high indexed facets accompanied by a general roundening of the particles. Furthermore, a strong decrease of (111)-type facet signals and a weak decrease of (110)-type facet signals - whose surface normal lies in the horizontal plane - point towards the shrinking of these facets when approaching the 10^{-3} mbar regime.

Moreover, under these conditions the intensity distribution along the (001)-rod appeared has varied. As can be viewed in the difference map the signal slightly decreased above and strongly increased below the Pt(111) Bragg peak. This indicates that the very top Pt layer was lifted up, probably due to strain effects caused by surface oxide formation or oxygen adsorption [70]. Furthermore, the Bragg peak position shifted towards a smaller reciprocal lattice value in out-of-plane

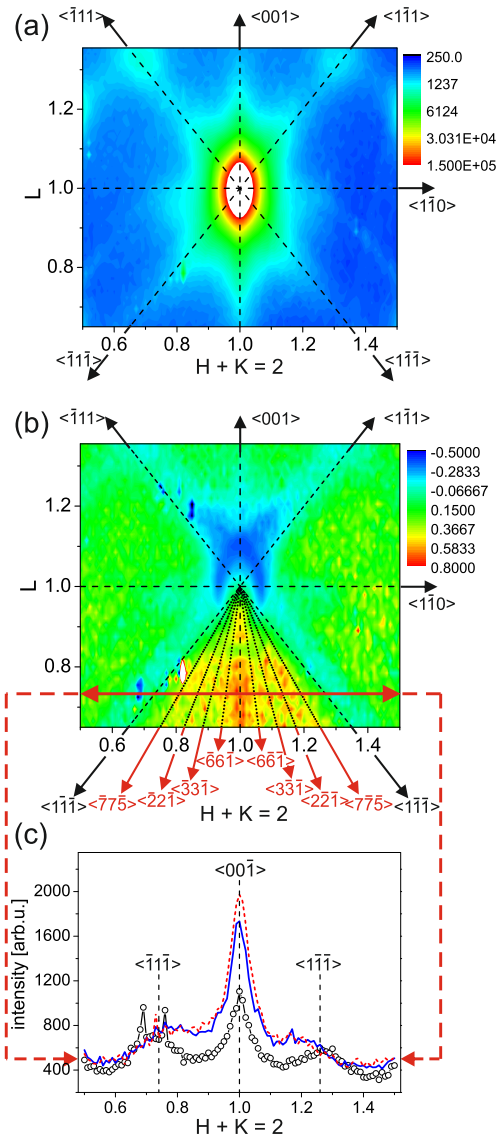

Fig. 6: (a): Reciprocal space map of sample I measured at 573 K in the (H+K=2,L)-plane after oxidizing to $6.5{\cdot}10^{-3}$ mbar; dashed lines indicate the calculated positions of (001)- and (111)-type facet signals. (b): difference map in the (H+K=2,L)-plane obtained by subtracting the map measured under oxidizing conditions from the map measured under UHV via $\frac{I_{UHV}-I_{10^{-3}mbar}}{I_{UHV}}$. As a guide to the eye expected positions of some higher indexed facet signals are indicated by dashed lines. (c): linescans at L=0.74 taken from the maps before (○) and after oxidizing (solid line) to $6.5{\cdot}10^{-3}$ mbar. The dashed line was taken from a map which was measured at 500 mbar oxygen pressure. The positions of (001)- and (111)-type facets are indicated by vertical dashed lines.

direction. This indicates that the out-of-plane Pt lattice parameter increased (Δa_{001}=0.028 $\AA$) and that oxygen adsorption or surface oxide formation not only had an impact on the Pt atoms at the very outside of the particles but also on the position of the inner Pt atoms. This finding is in accordance with a recent XRD study from Pt nanoparticle powders which disclosed that Pt diffraction peaks shifted to lower angles due to surface relaxations [71].

When increasing the oxygen pressure further to 500 mbar the intensity changes along the (001)-rod of sample I became even more pronounced since the intensity below the Pt Bragg peak increased further. Also the signals of higher indexed facets continued to slightly gain intensity. Still, it is evident that the main particle shape change took place in the 10^{-3} mbar oxygen pressure range.

On sample II the oxygen-induced shape changes were found to set in at an oxygen pressure of $1.1 \cdot 10^{-4}$ mbar at a temperature of 493 K (μ=-0.83 eV). As in the case of sample I the changes were characterized by the emergence of higher indexed facets and a decrease of signal intensity of the (111)-type facets. However, neither pronounced Bragg peak shifts nor any intensity variations along the (001)-rod were observed. Thus, we propose that for the on average larger particles of sample II oxygen adsorption and surface oxide formation had a much weaker impact on the atomic positions. This is in accordance with aforementioned XRD studies [71] that concluded peak shifts on Pt diffraction peaks to be inversely proportional to the particle size. However, one has to bear in mind that the different behavior of the two samples may not only be traced back to the different particle size but also to the significant differences in temperature and oxygen chemical potential during in-situ oxidation.

Our quantitative Bragg peak analysis finds the particle diameter and height under oxidizing conditions in the 10^{-3} mbar oxygen range to comprise D=61$\pm$6 $\AA$, H=45$\pm$8 $\AA$ in case of sample I and D=108$\pm$4 $\AA$, H=58$\pm$2 $\AA$ in case of sample II. The removal of one single Pt layer from fcc sites on top of a particle would correspond to a height decrease of 2 $\AA$. The size decrease deduced for the two samples is - if at all present - on the same order of magnitude (UHV: sample I: H=47$\pm$10 $\AA$, D=64$\pm$6 $\AA$; sample II: H=58$\pm$4 $\AA$, D=112$\pm$8 $\AA$). This supports the assumption that the particle shape changes were triggered off by thin surface oxides.

At 10^{-3} mbar oxygen pressure our x-ray reflectivity results find a particle height of 33.6 $\AA$ for sample I at 573 K and 48.1 $\AA$ for sample II at 493 K. These values are close to the ones found under UHV conditions which is in line with the small size changes deduced from our Bragg peak width analysis. Please note again the underestimation of particle height in the fit results of the reflectivity measurements (see supporting material).

Pt Bulk Oxide Formation

The oxygen-induced particle shape changes discussed in the previous section occurred for sample I at an oxygen chemical potential of μ=-0.92 eV (T=573 K, p_{O2}=4.0·10^{-3} mbar), for sample II at μ=-0.83 eV (T=493 K, p_{O2}=1.1·10^{-4} mbar). Under these conditions we could not detect any bulk oxide signals although according to DFT calculations [15] bulk oxides (Pt_3O_4 and α-PtO_2) should start to form at oxygen chemical potentials of μ=-0.85 eV or slightly higher. However, for sample II after having increased the temperature to 673 K (p_{O2}=1.1·10^{-4} mbar, μ=-1.06 eV) bulk oxide structure signals were found. This indicates that bulk oxide formation is kinetically hindered. Our experimental data can be understood by the coexistence of a hexagonal and a cubic oxide phase which we could identify as a modified version of (0001)-oriented α-PtO_2 and (110)-oriented Pt_3O_4 (see next paragraph; the corresponding bulk oxide unit cells are depicted in Fig. 9).

In order to determine the formed structures we performed reference scans in reciprocal space which are shown in Fig. 7(b),(c) and in Fig. 8. Fig. 7(a) indicates the position of the in-plane scans of Fig. 7(b) and (c) by solid lines labeled "A" and "B". In the rocking scan "A" of Fig. 7(b) oxide peaks appear every 30° and imply the formation of a hexagonal oxide structure with two domains. The reflections at ω=-125° and ω=-35° are much higher in intensity and are 90° apart which points to the existence of an additional oxide phase with two- or fourfold symmetry. Information on the out-of-plane structure of the bulk oxides was retrieved from L scans at distinct (H,K) values: the scan in Fig. 8(a) was obtained at position C in Fig. 7(a), probing the hexagonal bulk oxide only. The L scan at position D in Fig. 7(a) probes both the hexagonal and cubic oxide phase at the same

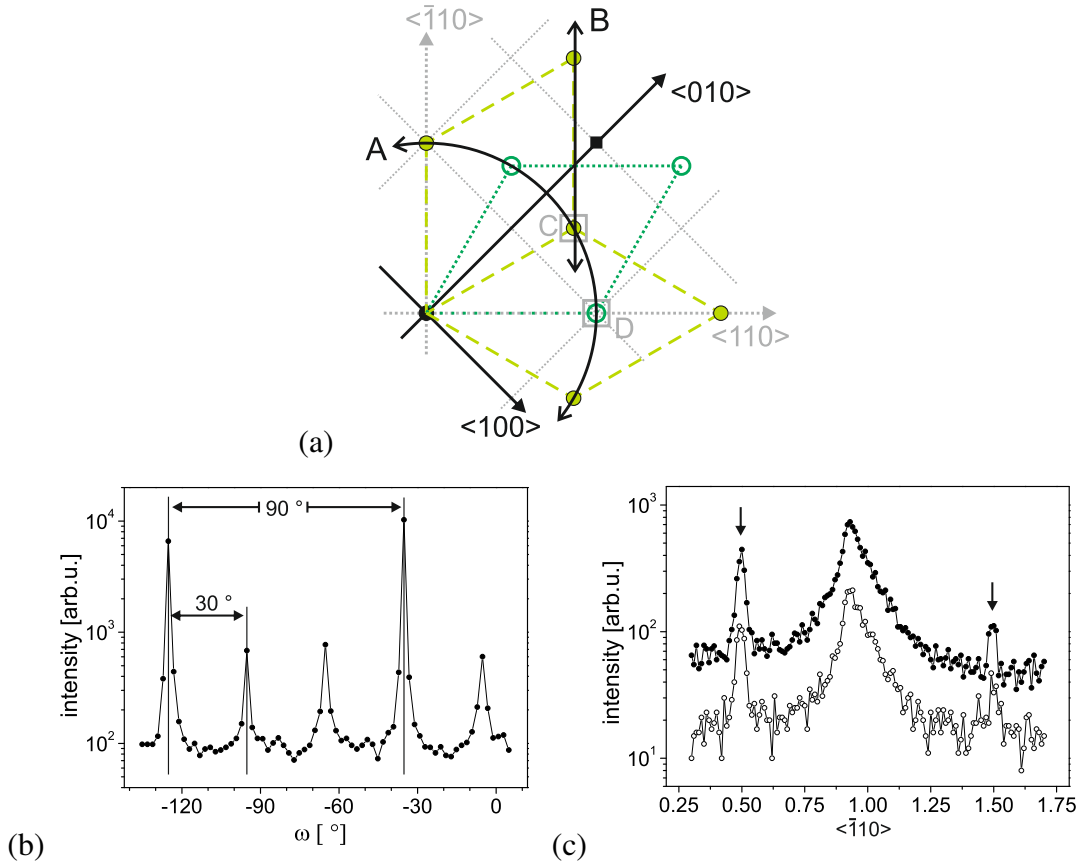

Fig. 7: (a): In-plane reciprocal space map indicating the scan directions of (b) and (c) as solid lines denoted by A and B; ○, ●: Bragg peaks of the two α-PtO_2 domains; ■: Pt Bragg peak of the $[100](001)_{Pt}$ || $[100](001)_{MgO}$-epitaxy; the peaks labeled C and D served as starting points for the out-of-plane scans in Fig. Figure 8. (b)+(c): in-plane-scans performed at T=673 K after oxidizing to $3.8{\cdot}10^{-3}$ mbar O_2 and subsequent annealing at 923 K for 40 minutes: (b): in-plane rocking scan A showing every 90° peaks of higher intensity (cubic oxide phase) and every 30° peaks of lower intensity (hexagonal oxide phase). (c): linescan at B displaying oxide peaks that belong to the hexagonal phase; the top curve (●) was measured directly after oxidizing to $3.8{\cdot}10^{-3}$ mbar, the lower scan (○) after additional annealing at 923 K.

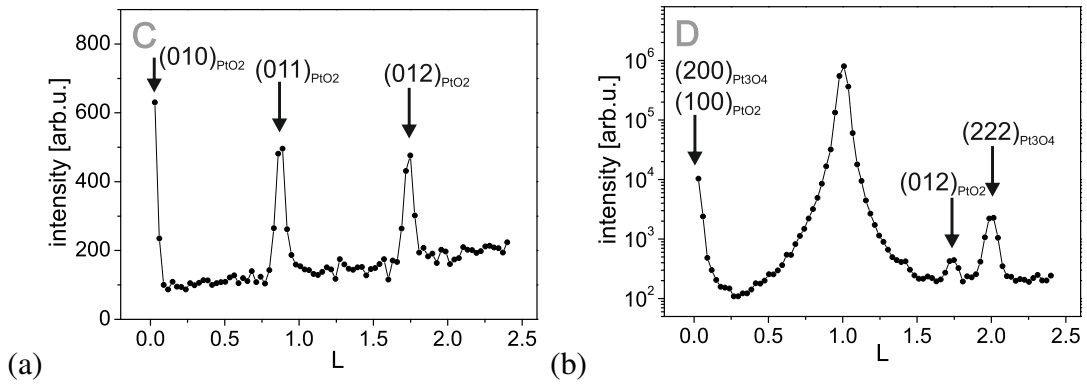

Fig. 8: Out-of-plane scans through oxide peaks from the hexagonal (a) and the cubic (b) oxide phase. Their in-plane starting points are labeled C and D in Fig. 7 (a). Oxide peaks are indicated by arrows, at L=1.0 in (b) the Pt (111) Bragg peak of the domain with $[100](001)_{Pt} \,||\, [100](001)_{MgO}$-epitaxy can be seen.

Table 1: As found in literature [40,72–74]: experimentally observed and DFT calculated (in parenthesis) lattice constants for Pt bulk oxide structures.

	α-PtO_2 [40,72]	Pt_3O_4 [40,72]	PtO [40,73]	β-PtO_2 [40,74]
structure	CdI_2, hexagonal	simple cubic	PdS, tetragonal	$CaCl_2$, orthorhombic
a [$\AA$]	3.10 (3.14)	5.59 (5.65)	3.08 (3.10)	4.48 (4.49)
b [$\AA$]	-	-	-	4.52 (4.71)
c [$\AA$]	4.28-4.40 (5.81)	-	5.34 (5.41)	3.14 (3.14)

time.

In order to identify the bulk oxide phases corresponding to the observed diffraction peaks we compared the experimental d-spacings, i.e. peak positions ("exp. d-spacings"), with structures found in literature ([40,72–74], see table 1). This comparison included the Pt bulk oxides α-PtO_2, Pt_3O_4, PtO and β-PtO_2. From our data we find the lattice parameters of the hexagonal oxide phase to be a=3.19 $\AA$ and c=4.49 $\AA$, which is in good agreement with the referenced experimental values for α-PtO_2 [40]. The hexagonal oxide's inplane lattice matches the Pt(100) surface, which explains the slight increase in a. The discrepancy between our experimentally obtained c value and the theoretically obtained one found in [72] may be explained by the intrinsic difficulty to calculate d-spacings for van-der-Waals bound layers, as present along the c axis in α-PtO_2. In support of

Table 2: Comparison between d-spacings obtained from our data ("exp. d-spacings") and obtained from experimental literature values of Pt bulk oxides [40]. Only for α-PtO_2 ("mod. α-PtO_2") the d-spacings were modified according to our experimentally found lattice constants a = 3.19 $\AA$ and c = 4.49 $\AA$. d-spacings belonging to peaks of the hexagonal and cubic peak pattern are indicated by h and c, respectively. Miller indices of corresponding scattering planes are shown in paranthesis; d-spacings of Pt_3O_4 and PtO peaks which would match peaks from the hexagonal phase are written in squared brackets.

peak coord. (hkl)	exp. d-spacings [$\AA$]	mod. α-PtO_2 [$\AA$]	SC Pt_3O_4 [$\AA$]	PtO [$\AA$]	β-PtO_2 [$\AA$]
(-0.37 1.37 0.00)	2.76^h	2.76 (010)	[2.80 (200)]	[2.67 (002)]	-
(-0.63 2.36 0.00)	1.60^h	1.60 ($\bar{1}$20)	-	-	-
(1.37 0.37 0.00)	2.76^h	2.76 (100)	[2.80 (200)]	[2.67 (002)]	-
(0.37 1.37 0.00)	2.76^h	2.76 (010)	[2.80 (200)]	[2.67 (002)]	-
(0.37 1.37 0.88)	2.35^h	2.35 (011)	-	-	-
(0.37 1.37 1.74)	1.75^h	1.74 (012)	-	-	-
(-1.00 1.00 0.00)	$2.76^{h,c}$	2.76 ($\bar{1}$10)	2.80 (200)	2.67 (002)	-
(1.00 1.00 0.00)	$2.76^{h,c}$	2.76 (100)	2.80 (200)	2.67 (002)	-
(1.00 1.00 2.00)	1.60^c	-	1.61 (222)	1.54 (020)	1.59 (220)
(1.00 1.00 1.74)	1.75^h	1.74 (012)	-	-	-

α-PtO_2 is moreover the fact that it is the only known hexagonal Pt oxide and thus the only structure that can explain the peak pattern found in the scans shown in Fig. 7 and Fig. 8. The mere consideration of the obtained d-spacings allows to rule out orthorhombic β-PtO_2 immediately.

Considering in table 2 the d-spacing values for the cubic bulk oxide phase one finds that both - Pt_3O_4 and PtO - could be possible candidates although the values of Pt_3O_4 match our experimentally obtained ones ("exp. d-spacings") better. However, PtO can fully be excluded since the spatial orientation of the Pt bulk oxide with respect to the found oxide peak positions only matches for Pt_3O_4 (see supporting material). Also the GeS-type structure, which was recently calculated to be the most stable structure for PtO [75], does not match our experimental data.

From the full width half maximum of the peaks belonging to the hexagonal and cubic oxide phase in the scans of Fig. 8 the oxide particle heights were estimated to H=56 $\AA$ and H=53 $\AA$, respectively. Taking into account the respective Pt atom density within and the respective volume of their corre-

sponding oxide unit cells the original Pt particle height and diameter amounted to H=21 $\mathring{A}$, D=41 $\mathring{A}$ (α-PtO_2) and H=27 $\mathring{A}$, D=53 $\mathring{A}$ (Pt_3O_4) before oxidation. Thus, we assume that the bulk oxides formed from the smaller nanoparticles whereas the larger paticles underwent the oxygen-induced shape changes discussed earlier. Such a size-dependent oxidation behaviour was also reported for other nanoparticle systems [54,76,77].

In order to study whether the oxygen-induced shape changes are reversible we exposed the oxidized samples to CO (sample I: $4.9 \cdot 10^{-4}$ mbar CO for ~20 min at 573 K; sample II: 1.2 mbar CO for ~20 min at 673 K): as can be concluded from Fig. 10 the linescans measured on the oxidized particles compared to the ones measured after CO exposure look very similar in case of both samples. Thus, we infer that CO did not have any impact on the shape of the oxidized particles and that no shape change reversibility occured. Even exposure to higher CO pressures (1.2 mbar) at elevated temperatures (T=673 K) as well as subsequent annealing at higher temperatures (once at 903 K for 35 minutes before CO exposure and once at 923 K for 35 minutes after CO exposure) as performed on sample II did not lead to a shape change reversibility. Pursuant to these observations we conclude that the surface oxides formed on the particle facets are kinetically very stable and are not very reactive towards CO oxidation.

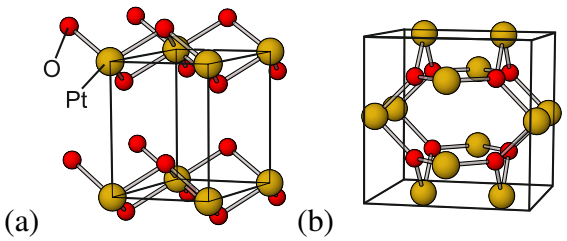

Fig. 9: Unit cells of (a): modified α-PtO_2 (a=3.19 $\mathring{A}$, c=4.49 $\mathring{A}$) - (b): simple cubic Pt_3O_4 (a=5.59 $\mathring{A}$).

Furthermore, we find that the Pt bulk oxide structures are thermally very stable. The top curve in Fig. 7(c) was measured directly after oxidizing to $3.8 \cdot 10^{-3}$ mbar oxygen pressure whereas the bottom curve was recorded after an additional annealing cycle at 923 K for ~40 minutes. Subsequent to this annealing bulk oxide signals at 0.5 and 1.5 in $\langle \bar{1}10 \rangle$ direction were still present.

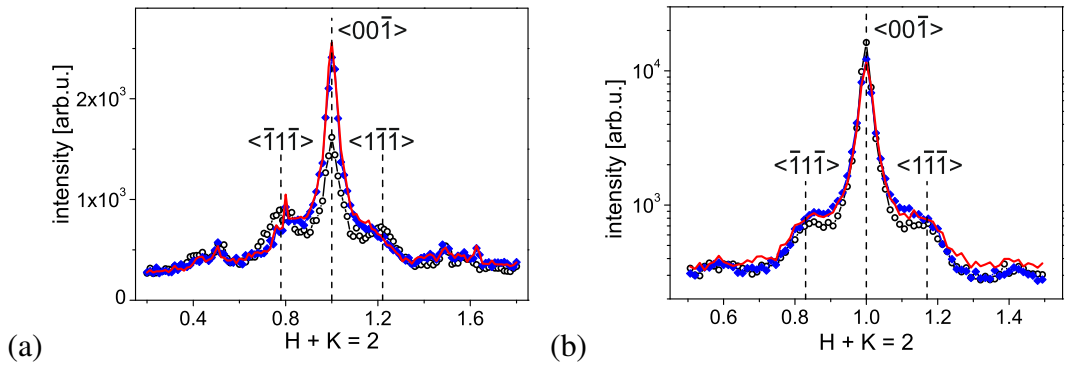

Fig. 10: Linescans measured on sample I (a) at L=0.78 and sample II (b) at L=0.83 under UHV conditions (○; sample I: T=573 K; sample II: T=593 K), under oxidizing conditions (◆; sample I: T=573 K, p=500 mbar O_2; sample II: T=493 K, p=$1.53 \cdot 10^{-3}$ mbar O_2) and after CO exposure (solid line; sample I: T=573 K, p=$4.9 \cdot 10^{-4}$ mbar CO; sample II: T=673 K, p=1.2 mbar CO).

Discussion

According to our data additional annealing after Pt deposition leads to on average larger particles, a wider particle size distribution and to polycrystalline Pt. The latter was found to result in additional smaller particles upon subsequent annealing. We propose that the wider size distribution and the on average larger particles on sample II can be traced back to Ostwald-ripening during annealing after deposition. Our data show that the percentage of (111)-oriented particles is higher on this additionally annealed sample. This is in disagreement with results of previous studies in which additional annealing after deposition resulted in particles favouring cube-on-cube epitaxy [57]. On the other hand in our case the particles on the extra annealed sample II are on average larger than on sample I. Thus, the (111)-orientation is likely to be energetically more favorable for the particles of sample II [63–65].

In the following our experimental findings on the particle shape and oxygen-induced shape changes will be compared to the theoretical results in [15]. In this comparison it has to be taken into account that the theoretical calculations only consider a limited number of possible particle facet orientations and that they were performed for unsupported particles.

As proposed by theory the equilibrium particle shape under UHV conditions consists of (111)- and (001)-type facets decorated by some higher indexed facets which is in good accordance with

our experimental findings. By simulating the reciprocal space map under UHV conditions we obtained a ratio of the surface energies belonging to the (001)- and (111)-type facets which amounts to $(\frac{\gamma_{001}}{\gamma_{111}})_{exp}=\sqrt{3}\cdot\frac{13\pm2}{23\pm2}=0.98\pm0.26$. For the theoretically calculated surface energies this ratio yields $(\frac{\gamma_{001}}{\gamma_{111}})_{unr}=1.215$ in the case of an unreconstructed Pt(001) top facet while assuming a (1×5) reconstruction results in a ratio of $(\frac{\gamma_{001}}{\gamma_{111}})_{rec}=1.054$. Since the latter value is closer to the experimentally obtained one we propose that reconstructions form on the (001)-type facets to lower their surface energy as is the case on (001) single crystal surfaces. This is in line with previous experimental SEM studies performed on micron-sized Pt particles which revealed that the surface energy of Pt(100)-type facets is comparable and even lower than the one of Pt(111)-facets.[78]

Experimentally we found that the oxygen-induced shape changes set in at $4.0\cdot10^{-3}$ mbar (T=573 K) and at $1.1\cdot10^{-4}$ mbar (T=493 K), respectively. This corresponds to the respective oxygen chemical potentials of μ=-0.92 eV and -0.83 eV. The emergence of higher indexed facets at the expense of the size of the (111)-type facets which we deduced from our experimental findings is in accordance with theoretical expectations [15]. These results are moreover in line with environmental high resolution electron microscope (ETEM) studies that concluded a particle roundening linked to a decrease of (111) particle facets under oxidizing conditions [79]. However, while ETEM traces the performance of limited local particle ensembles our SXRD studies probed large sample areas and thus enabled to determine the average particle behavior on the samples. Contrary to our findings theory proposes the first shape changes to occur at an oxygen chemical potential of μ=-1.4 eV and suggests a round particle shape already at μ=-1.2 eV. We assume that the experimentally found delay of the particle shape change when going to higher oxygen pressures can be explained by kinetically hindered oxygen adsorption or surface oxide formation. At a chemical potential of μ=-1.0 eV theory expects the nanoparticles to consist of mainly (111)- and (110)-type facets. According to our experimental findings, however, the (110)-type facets rather seem to decrease in size when approaching this chemical potential. Thus, we come to the conclusion that the stability of the (12×2)-reconstruction on the (110)-type facets might be overestimated or that the formation of the reconstruction might not take place on nanosized particles due to geometrical constraints. A

further difference can be seen in the fact that for a chemical potential of μ=-1.0 eV theory expects the (001)-type facets to be negligibly small since dereconstruction of the (001)-surface is expected to cost much energy. From our experiments, however, we concluded under these conditions and even at higher chemical potentials the nanoparticles to still be dominated by (001)-type facets.

Since we evidenced bulk oxide formation on sample II after increasing the temperature from 493 K to 673 K we assume that it is kinetically hindered at lower temperatures as proposed in [41,42]. At 673 K bulk oxides were present at an oxygen pressure of $3.8 \cdot 10^{-3}$ mbar (μ=-1.06 eV) and thus even at lower chemical oxygen potentials than theoretically expected (μ_{theo}=-0.85 eV [15]). Apart from the temperature as main driving force we propose that also the particle size may play a role in bulk oxide formation which is in good accordance with other results supporting size-dependent bulk oxide formation for nanoparticle systems [54,76,77]: we assume that only the smallest particles with H$\leq$30 $\AA$ - present only significantly on sample II due to its wider particle size distribution - became fully oxidized under the aforementioned conditions. We propose that the surface oxides on the larger particles of sample II may act as protection against bulk oxide formation which in turn might also at 673 K still be kinetically hindered [41,42,80,81]. On sample I we were not able to observe any bulk oxide signals at oxygen pressures as high as 500 mbar and a temperature of 573 K (μ=-0.595 eV). Also in this case we assume precursor-mediated kinetics for which surface oxides inhibit bulk oxide formation which is moreover kinetically hindered due to too low temperatures.

Our results clearly show that the majority of bulk oxides formed on sample II displayed the structure of (110)-oriented Pt_3O_4 which disagrees with DFT studies according to which α-PtO_2 bulk oxides are regarded to be thermodynamically more stable, especially for smaller particles [82]. Our findings partially agree with a recent XPS study on oxidized Pt nanoparticles in which α-PtO_2 and PtO were assigned to be the formed bulk oxides [54]. Whereas it is not possible to distinguish between Pt_3O_4 and PtO_2 species by uniquely regarding XPS binding energies [54–56] our XRD results provide crucial structural information. However, it also has to be taken into account that the Pt nanoparticles in the aforementioned XPS study are of no specific epitaxy and that the particle bulk oxides were obtained by O_2 plasma exposure at room temperature which complicates the compar-

ison to our results.

It is striking that the portion of the cubic bulk oxides (79 %) compared to the one of the hexagonal phases (21 %) corresponds well to the portion of particles growing with cube-on-cube epitaxy (85 %) compared to the ones growing with a (111)-orientation (15 %). Particles with cube-on-cube epitaxy expose large (001)-type facets which should facilitate the growth of cubic Pt_3O_4 [40]. Thus a tentative explanation could be that Pt_3O_4 starts to form for particles with cube-on-cube epitaxy while hexagonal α-PtO_2 might form on particles growing with hexagonal (111)-type epitaxies. However, it has to be taken into account that the (001)-oriented MgO substrate might influence the resulting particle bulk oxide structure leading to a higher percentage of cubic Pt_3O_4.

The high thermal stability which we found for our oxidized particles is in agreement with previous studies on oxidized Pt nanoparticles [41,54]. It was assumed that kinetic barriers stabilize the Pt oxide particles against thermal decomposition [41]. Particle size-dependent thermal stability was observed in a XPS and TPD study: the highest oxygen desorption temperatures were found for 2 nm-sized nanoparticles at temperatures of 921 - 925 K [54]. In a previous XPS study traces of PtO were observed even up to 1000 K [83].

Conclusions

In summary, we studied oxygen-induced shape changes and bulk oxide formation of MgO(001)-supported Pt nanoparticles by means SXRD, XRR and complementary TEM measurements. We found the equilibrium particle shape under UHV conditions mainly to consist of (111)-and (001)-type facets and thus to be close to the shape obtained from the Wulff-Kashiew construction when taking into account reconstructions on the (001)-type particle facets.

The main oxygen-induced shape changes on the two samples were found to occur at oxygen pressures of $4.0 \cdot 10^{-3}$ mbar (T=573 K) and at $1.1 \cdot 10^{-4}$ mbar (T=493 K), respectively. They were characterized by the formation of higher indexed facets at the expense of (111)-type facets. These shape changes were induced by surface oxides and set in at higher oxygen chemical potentials

than theoretically expected. This indicates that surface oxide formation is kinetically hindered at the aforementioned temperatures. A kinetic hindrance also explains the fact that it was a higher temperature of 673 K (p_{O2}=3.8·10^{-3} mbar) at which bulk oxides were inferred to have formed. We concluded that only smaller particles (H$\leq$30 $\AA$) became fully oxidized. Two domains of (110)-oriented Pt_3O_4 and two domains of (0001)-oriented α-PtO_2 bulk oxides were found to coexist and appeared to be thermally very stable since they could not be removed by repeated annealing at 923 K. In contrast to the results found for MgO(001)-supported Rh and Pd nanoparticles CO exposure of the oxidized Pt particles did not lead to a shape change reversibility [14,17]. This indicates that the formed oxides might be inactive in CO oxidation reactions.

Acknowledgement

The authors thank the Stuttgart Center for Electron Microscopy (StEM) of the MPI for intelligent systems for TEM sample preparation and characterization (M. Kelsch, P. Kopold, P.A. van Aken). Financial support by the BMBF (project 05K10PS1 NanoXcat) is gratefully acknowledged.

Supporting Information Available

The Supporting Information contains additional details about the underlying fit model of the x-ray reflectivity data and the consequential data interpretation, the analysis of the TEM plain view images, the quantitative particle size and shape analysis (Bragg peak analysis and reciprocal space map analysis) and the identification of the bulk oxide structures. This information is available free of charge via the Internet at http://pubs.acs.org.

References

(1) Gandhi, H. S.; Graham, G. W.; McCabe, R. W. Automotive Exhaust Catalysis. *J. of Cat.* **2003**, *216*, 433–442.

(2) Roldaán Cuenya, B. Synthesis and Catalytic Properties of Metal Nanoparticles: Size, Shape, Support, Composition, and Oxidation State Effects. *Thin Solid Films* **2010**, *518*, 3127–3150.

(3) Mehta, V.; Smith Cooper, J. Review and Analysis of PEM Fuel Cell Design and Manufacturing. *Journal of Power Sources* **2003**, *114*, 32–53.

(4) Park, D.-H.; Jeon, Y.; Ok, J.; Park, J.; Yoon, S.-H.; Choy, J.-H.; Shul, Y.-G. Pt Nanoparticle-Reduced Graphene Oxide Nanohybrid for Proton Exchange Membrane Fuel Cells. *Journal of Nanoscience and Nanotechnology* **2012**, *12*, 5669–5672.

(5) Greco, G.; Witkowska, A.; Minicucci, M.; Olivi, L.; Principi, E.; Dsoke, S.; Moretti, A.; Marassi, R.; Di Cicco, A. Local Ordering Changes in Pt-Co Nanocatalyst Induced by Fuel Cell Working Conditions. *J. Phys. Chem. C* **2012**, *116*, 12791–12802.

(6) Imai, H.; Izumi, K.; Matsumoto, M.; Kubo, Y.; Kato, K.; Imai, Y. In Situ and Real-Time Monitoring of Oxide Growth in a Few Monolayers at Surfaces of Platinum Nanoparticles in Aqueous Media. *J. Am. Chem. Soc.* **2009**, *131*, 6293–6300.

(7) Friebel, D.; Viswanathan, V.; Miller, D. J.; Anniyev, T.; Ogasawara, H.; Larsen, A. H.; O'Grady, C. P.; Norskov, J. K.; Nilsson, A. Balance of Nanostructure and Bimetallic Interactions in Pt Model Fuel Cell Catalysts: In Situ XAS and DFT Study. *J. Am. Chem. Soc.* **2012**, *134*, 9664–9671.

(8) Holby, E. F.; Greeley, J.; Morgan, D. Thermodynamics and Hysteresis of Oxide Formation and Removal on Platinum (111) Surfaces. *J. Phys. Chem. C* **2012**, *116*, 9942–9946.

(9) Callejas-Tovar, R.; Liao, W.; Mera, H.; Balbuena, P. B. Molecular Dynamics Simulations of Surface Oxidation on Pt and Pt/PtCo/Pt_3Co Nanoparticles Supported over Carbon. *J. Phys. Chem. C* **2011**, *115*, 23768–23777.

(10) Pöpke, H.; Mutoro, E.; Luerssen, B.; Janek, J. Oxidation of Platinum in the Epitaxial Model

System Pt(111)/YSZ(111): Quantitative Analysis of an Electrochemically Driven PtO_x Formation. *J. Phys. Chem. C* **2012**, *116*, 1912–1920.

(11) Freund, H.-J.; Bäumer, M.; Libuda, J.; Risse, T.; Rupprechter, G.; Shaikhutdinov, S. Preparation and Characterization of Model Catalysts: from Ultrahigh Vacuum to In Situ Conditions at the Atomic Dimension. *J. of Cat.* **2003**, *216*, 223–235.

(12) Henry, C. R. Surface Studies of Supported Model Catalysts. *Surf. Sci. R.* **1998**, *31*, 231–325.

(13) Zaera, F. New Challenges in Heterogeneous Catalysis for the 21st Century. *Cat. Lett.* **2012**, *142*, 501–516.

(14) Nolte, P.; Stierle, A.; Jin-Phillipp, N. Y.; Kasper, N.; Schulli, T. U.; Dosch, H. Shape Changes of Supported Rh Nanoparticles During Oxidation and Reduction Cycles. *Science* **2008**, *321*, 1654–1658.

(15) Seriani, N.; Mittendorfer, F. Platinum-Group and Noble Metals under Oxidizing Conditions. *J. Phys.: Condens. Matter* **2008**, *20*, 184023–184033.

(16) Mostafa, S.; Behafarid, F.; Croy, J. R.; Ono, L. K.; Li, L.; Yang, J. C.; Frenkel, A. I.; Roldán Cuenya, B. Shape-Dependent Catalytic Properties of Pt Nanoparticles. *J. Am. Chem. Soc.* **2010**, *132*, 15714–15719.

(17) Nolte, P.; Stierle, A.; Kasper, N.; Jin-Phillipp, N. Y.; Jeutter, N.; Dosch, H. Reversible Shape Changes of Pd Nanoparticles on MgO(100). *Nano Lett.* **2011**, *11*, 4697–4700.

(18) Mars, P.; van Krevelen, D. W. Oxidations Carried Out by means of Vanadium Oxide Catalysts. *Spec. Suppl. Chem. Eng. Sci.* **1954**, *3*, 41–59.

(19) Hendriksen, B. L. M.; Frenken, J. W. M. CO Oxidation on Pt(110): Scanning Tunneling Microscopy inside a High-Pressure Flow Reactor. *Phys. Rev. Lett.* **2002**, *89*, 046101–1 – 046101–4.

(20) Wintterlin, J.; Völkening, S.; Janssens, T. V. W.; Zambelli, T.; Ertl, G. Atomic and Macroscopic Reaction Rates of a Surface-Catalyzed Reaction. *Science* **1997**, *278*, 1931–1934.

(21) Campbell, C. T.; Ertl, G.; Kuipers, H.; Segner, J. A Molecular Beam Study of the Catalytic Oxidation of CO on a Pt(111) Surface. *J. Chem. Phys.* **1980**, *73*, 5862–5873.

(22) McClure, S. M.; Goodman, D. W. New Insights into Catalytic CO Oxidation on Pt-Group Metals at Elevated Pressures. *Chem. Phys. Lett.* **2009**, *469*, 1–13.

(23) Chung, J.-Y.; Aksoy, F.; Grass, M. E.; Kondoh, H.; Ross Jr., P.; Liu, Z.; Mun, B. S. In-Situ Study of the Catalytic Oxidation of CO on a Pt(110) Surface Using Ambient Pressure X-Ray Photoelectron Spectroscopy. *Surf. Science* **2009**, *603*, L35–L38.

(24) Ackermann, M. D.; Pedersen, T. M.; Hendriksen, B. L. M.; Robach, O.; Bobaru, S. C.; Popa, I.; Quirós, C.; Kim, H.; Hammer, B.; Ferrer, S.; Frenken, J. W. M. Structure and Reactivity of Surface Oxides on Pt(110) During Catalytic CO Oxidation. *Phys. Rev. Lett.* **2005**, *95*, 255505–1–255505–4.

(25) Butcher, D. R.; Grass, M. E.; Zeng, Z.; Aksoy, F.; Bluhm, H.; Li, W.-X.; Mun, B. S.; Somorjai, G. A.; Liu, Z. In Situ Oxidation Study of Pt(110) and its Interaction with CO. *J. Am. Chem. Soc.* **2011**, *133*, 20319–20325.

(26) Allian, A. D.; Takanabe, K.; Fujdala, K. L.; Hao, X.; Truex, T. J.; Cai, J.; Buda, C.; Neurock, M.; Iglesia, E. Chemisorption of CO and Mechanism of CO Oxidation on Supported Platinum Nanoclusters. *J. Am. Chem. Soc.* **2011**, *133*, 4498–4517.

(27) Dobrin, S. CO Oxidation on Pt Nanoclusters, Size and Coverage Effects: a Density Functional Theory Study. *Phys. Chem. Chem. Phys.* **2012**, *14*, 12122–12129.

(28) Steininger, H.; Lehwald, S.; Ibach, H. Adsorption of Oxygen on Pt(111). *Surf. Science* **1982**, *123*, 1–17.

(29) Parker, D. H.; Bartram, M. E.; Koel, B. E. Study of High Coverages of Atomic Oxygen on the Pt(111) Surface. *Surf. Science* **1989**, *217*, 489–510.

(30) Weaver, J. F.; Chen, J.-J.; Gerrard, A. L. Oxidation of Pt(111) by Gas-Phase Oxygen Atoms. *Surf. Science* **2005**, *592*, 83–103.

(31) Wintterlin, J.; Schuster, R.; Ertl, G. Existence of a ŞHotŤ Atom Mechanism for the Dissociation of O_2 on Pt(111). *Phys. Rev. Lett.* **1996**, *77*, 123–126.

(32) Materer, N.; Starke, U.; Barbieri, A.; Döll, R.; Heinz, K.; Van Hove, M. A.; Somorjai, G. A. Reliability of Detailed LEED Structural Analyses: Pt(111) and Pt(111)-p(2x2)-O. *Surf. Science* **1995**, *325*, 207–222.

(33) Devarajan, S. P.; Hinojosa Jr., J. A.; Weaver, J. F. STM Study of High-Coverage Structures of Atomic Oxygen on Pt(111): p(2 x 1) and Pt Oxide Chain Structures. *Surf. Science* **2008**, *602*, 3116–3124.

(34) Ellinger, C.; Stierle, A.; Robinson, I. K.; Nefedov, A.; Dosch, H. Atmospheric Pressure Oxidation of Pt(111). *J. Phys.: Condens. Matter* **2008**, *20*, 184013–1 – 184013–5.

(35) Miller, D. J.; Öberg, H.; Kaya, S.; Sanchez Casalongue, H.; Friebel, D.; Anniyev, T.; Ogasawara, H.; Bluhm, H.; Pettersson, L. G. M.; Nilsson, A. Oxidation of Pt(111) under Near-Ambient Conditions. *Phys. Rev. Lett.* **2011**, *107*, 195502–1 – 195502–5.

(36) Krasnikov, S. A.; Murphy, S.; Berdunov, N.; McCoy, A. P.; Radican, K.; Shvets, I. V. Self-Limited Growth of Triangular PtO_2 Nanoclusters on the Pt(111) Surface. *Nanotechnology* **2010**, *21*, 335301–1 – 335301–7.

(37) Bandlow, J.; Kaghazchi, P.; Jacob, T.; Papp, C.; Tr$^{\acute{}}$ankenschuh, B.; Streber, R.; Lorenz, M. P. A.; Fuhrmann, T.; Denecke, R.; Steinrück, H.-P. Oxidation of Stepped Pt(111) Studied by X-Ray Photoelectron Spectroscopy and Density Functional Theory. *Phys. Rev. B* **2011**, *83*, 174107–7–174107–5.

(38) Hawkins, J. M.; Weaver, J. F.; Asthagiri, A. Density Functional Theory Study of the Initial Oxidation of the Pt(111) Surface. *Phys. Rev. B* **2009**, *79*, 125434–1 – 125434–13.

(39) Pang, Q.; Zhang, Y.; Zhang, J.-M.; Xu, K.-W. Structural and Electronic Properties of Atomic Oxygen Adsorption on Pt(111): A Density-Functional Theory Study. *Appl. Surf. Science* **2011**, *257*, 3047–3054.

(40) Seriani, N.; Pompe, W.; Colombi Ciacchi, L. Catalytic Oxidation Activity of Pt_3O_4 Surfaces and Thin Films. *J. Phys. Chem. B* **2006**, *110*, 14860–14869.

(41) Weaver, J. F.; Kan, H. H.; Shumbera, R. B. Growth and Properties of High-Concentration Phases of Atomic Oxygen on Platinum Single-Crystal Surfaces. *J. Phys.: Condens. Matter* **2008**, *20*, 184015–1 – 184015–11.

(42) Shumbera, R. B.; Kan, H. H.; Weaver, J. F. The Transition from Surface to Bulk Oxide Growth on Pt(100): Precursor-Mediated Kinetics. *Surf. Science* **2007**, *601*, 4809–4816.

(43) Griffiths, K.; Jackman, T. E.; Davies, J. A.; Norton, P. R. Interaction of O_2 with Pt(100). *Surf. Science* **1984**, *138*, 113–124.

(44) Shumbera, R. B.; Kan, H. H.; Weaver, J. F. Adsorption of Gas-Phase Oxygen Atoms on Pt(100)-hex-R0.7°: Evidence of a Metastable Chemisorbed Phase. *Surf. Science* **2006**, *600*, 2928–2937.

(45) Deskins, N. A.; Lauterbach, J.; Thomson, K. T. Lifting the Pt100 Surface Reconstruction through Oxygen Adsorption: A Density Functional Theory Analysis. *J. Chem. Phys.* **2005**, *122*, 184709–1–184709–8.

(46) Li, W. X.; Österlund, L.; Vestergaard, E. K.; Vang, R. T.; Matthiesen, J.; Pedersen, T. M.; Laegsgaard, E.; Hammer, B.; Besenbacher, F. Oxidation of Pt(110). *Phys. Rev. Lett.* **2004**, *93*, 146104–1 – 146104–4.

(47) Pedersen, T. M.; Li, W. X.; Hammer, B. Structure and Activity of Oxidized Pt(110) and α-PtO_2. *Phys. Chem. Chem. Phys.* **2006**, *8*, 1566–1574.

(48) Li, W.-X. Oxidation of Platinum Surfaces and Reaction with Carbon Monoxide. *J. Phys.: Condens. Matter* **2008**, *20*, 184022–1 – 184022–7.

(49) Zhu, Z.; Tao, F. F.; Zheng, F.; Chang, R.; Li, Y.; Heinke, L.; Liu, Z.; Salmeron, M.; Somorjai, G. A. Formation of Nanometer-Sized Surface Platinum Oxide Clusters on a Stepped Pt(557) Single Crystal Surface Induced by Oxygen: A High- Pressure STM and Ambient-Pressure XPS Study. *Nano Lett.* **2012**, *12*, 1491–1497.

(50) Wang, J. G.; Li, W. X.; Borg, M.; Gustafson, J.; Mikkelsen, A.; Pedersen, T. M.; Lundgren, E.; Weissenrieder, J.; Klikovits, J.; Schmid, M.; Hammer, B.; Andersen, J. N. One-Dimensional PtO_2 At Pt Steps: Formation and Reaction with CO. *Phys. Rev. Lett.* **2005**, *95*, 256102–1 – 256102–4.

(51) Wulff, G. Zur Frage der Geschwindigkeit des Wachsthums und der Auflösung der Krystallflächen. *Z. Kristallogr.* **1901**, *34*, 449–530.

(52) Vlad, A.; Stierle, A.; Westerström, R.; Blomberg, S.; Mikkelsen, A.; Lundgren, E. Oxygen Interaction with the Pd(112) Surface: From Chemisorption to Bulk Oxide Formation. *Phys. Rev. B* **2012**, *86*, 035407–1 – 035407–9.

(53) Vayssilov, G. N.; Lykhach, Y.; Migani, A.; Staudt, T.; Petrova, G. P.; Tsud, N.; Skála, T.; Bruix, A.; Illas, F.; Prince, K. C.; Matolín, V.; Neyman, K. M.; Libuda, J. Support Nanostructure Boosts Oxygen Transfer to Catalytically Active Platinum Nanoparticles. *Nat. Mater.* **2011**, *10*, 310–315.

(54) Ono, L. K.; Croy, J. R.; Heinrich, H.; Roldán Cuenya, B. Oxygen Chemisorption, Formation, and Thermal Stability of Pt Oxides on Pt Nanoparticles Supported on SiO_2/Si(001): Size Effects. *J. Phys. Chem. C* **2011**, *115*, 16856–16866.

(55) Shumbera, R. B.; Kan, H. H.; Weaver, J. F. Oxidation of Pt(100)-hex-R0.7° by Gas-Phase Oxygen Atoms. *Surf. Science* **2007**, *601*, 235–246.

(56) Kuribayashi, K.; Kitamura, S. Preparation of Pt-PtO_x Thin Films as Electrode for Memory Capacitors. *Thin Solid Films* **2001**, *400*, 160–164.

(57) Olander, J.; Lazzari, R.; Jupille, J.; Mangili, B.; Goniakowski, J. Size- and Temperature-Dependent Epitaxy for a Strong Film-Substrate Mismatch: the Case of Pt/MgO(001). *Physical Review B* **2007**, *76*, 075409–1 – 075409–16.

(58) Cillessen, J. F. M.; Wolf, R. M.; de Leeuw, D. M. Pulsed Laser Deposition of Heteroepitaxial Thin Pt Films on MgO(100). *Thin Solid Films* **1993**, *226*, 53–58.

(59) McIntyre, P. C.; Maggiore, C. J.; Nastasi, M. Orientation Selection in Thin Platinum Films on (001) MgO. *J.Appl. Phys.* **1995**, *77*, 6201–6204.

(60) Goniakowski, J.; Jelea, A.; Mottet, C.; Barcaro, G.; Fortunelli, A.; Kuntová, Z.; Nita, F.; Levi, A. C.; Rossi, G.; Ferrando, R. Structures of Metal Nanoparticles Adsorbed on MgO(001). II. Pt and Pd. *J. Chem. Phys.* **2009**, *130*, 174703–1 – 174703–9.

(61) Scavia, G.; Agostinelli, E.; Laureti, S.; Varvaro, G.; Paci, B.; Generosi, A.; Albertini, V. R.; Kaciulis, S.; Mezzi, A. Evolution of the Pt Layer Deposited on MgO(001) by Pulsed Laser Deposition as a Function of the Deposition Parameters: A Scanning Tunneling Microscopy and Energy Dispersive X-Ray Diffractometry/Reflectometry Study. *J. Phys. Chem. B* **2006**, *110*, 5529–5536.

(62) Lairson, B. M.; Visokay, M. R.; Sinclair, R.; Hagstrom, S.; Clemens, B. M. Epitaxial Pt(001), Pt(110), And Pt(111) Films on MgO(001), MgO(110), MgO(111), and Al_2O_3(0001). *Appl. Phys. Lett.* **1992**, *61*, 1390–1392.

(63) McIntyre, P. C.; Maggiore, C. J.; Nastasi, M. Epitaxy of Pt Thin Films on (001) MgO–I. Interface Energetics and Misfit Accomodation. *Acta Materialia* **1997**, *45*, 869–878.

(64) McIntyre, P. C.; Maggiore, C. J.; Nastasi, M. Epitaxy of Pt Thin Films On (001) MgO–II: Orientation Evolution from Nucleation through Coalescence. *Acta Materialia* **1997**, *45*, 879–887.

(65) Gatel, C.; Baules, P.; Snoeck, E. Morphology of Pt Islands Grown on MgO(001). *J. Cryst. Growth* **2003**, *252*, 424–432.

(66) Stierle, A.; Steinhäuser, A.; Rühm, A.; Renner, F. U.; Weigel, R.; Kasper, N.; Dosch, H. Dedicated Max-Planck Beamline for the *In Situ* Investigation of Interfaces and Thin Films. *Rev. Sci. Instr.* **2004**, *75*, 5302–5307.

(67) Kasper, N.; Stierle, A.; Jin-Phillipp, Y.; Wagner, T.; de Oteyza, D. G.; Dosch, H. In Situ Oxidation Study of MgO(100) Supported Pd Nanoparticles. *Surf. Science* **2006**, *600*, 2860–2867.

(68) Jin-Phillipp, N. Y.; Nolte, P.; Stierle, A.; Dosch, H. Initial Oxidation of MgO-Supported Rh Nanoparticles Studied by TEM. *Surf. Science* **2009**, *603*, 2551–2555.

(69)

(70) Robinson, I. K.; Tweet, D. J. Surface X-ray Diffraction. *Rep. Prog. Phys.* **1992**, *55*, 599–651.

(71) Rzeszotarski, P.; Kaszkur, Z. Surface Reconstruction of Pt Nanocrystals Interacting with Gas Atmosphere. Bridging the Pressure Gap with In Situ Diffraction. *Phys. Chem. Chem. Phys.* **2009**, *11*, 5416–5421.

(72) Muller, O.; Roy, R. Formation and Stability of the Platinum and Rhodium Oxides at High Oxygen Pressures and the Structures of Pt_3O_4, β-PtO_2 and RhO_2. *J. Less-Common Metals* **1968**, *16*, 129–146.

(73) McBride, J. R.; Graham, G. W.; Peters, C. R.; Weber, W. H. Growth and Characterization of Reactively Sputtered Thinfilm Platinum Oxides. *J. Appl. Phys.* **1991**, *69*, 1596–1604.

(74) Weber, W. H.; Graham, G. W.; McBride, J. R. Raman Spectrum of β-$Pt0_2$. Evidence for the $D^{12}{}_{2h}$-to-$D^{14}{}_{4h}$ Phase Transition. *Phys. Rev. B* **1990**, *42*, 10969–10975.

(75) Nomiyama, R. K.; Piotrowski, M. J.; Da Silva, J. L. F. Bulk Structures of PtO and PtO_2 from Density Functional Calculations. *Phys. Rev. B* **2011**, *84*, 100101–1 – 100101–4.

(76) Nolte, P.; Stierle, A.; Kasper, N.; Jin-Phillipp, N. Y.; Reichert, H.; Rühm, A.; Okasinski, J.; Dosch, H.; Schöder, S. Combinatorial High-Energy X-Ray Microbeam Study of the Size-Dependent Oxidation of Pd Nanoparticles on MgO(100). *Phys. Rev. B* **2008**, *77*, 115444–1 – 115444–7.

(77) Putna, E. S.; Vohs, J. M.; Gorte, R. J. Oxygen Desorption from α-Al_20_3 (0001) Supported Rh, Pt and Pd Particles. *Surf. Sci. Lett.* **1997**, *391*, L1178–L1182.

(78) Lee, W. H.; Vanloon, K. R.; Petrova, V.; Woodhouse, J. B.; Loxton, C. M.; Masel, R. I. The Equilibrium Shape and Surface Energy Anisotropy of Clean Platinum. *J. of Cat.* **1990**, *126*, 658–671.

(79) Cabié, M.; Giorgio, S.; Henry, C. R.; Axet, M. R.; Philippot, K.; Chaudret, B. Direct Observation of the Reversible Changes of the Morphology of Pt Nanoparticles under Gas Environment. *J. Phys. Chem. C* **2010**, *114*, 2160–2163.

(80) Gustafson, J.; Mikkelsen, A.; Borg, M.; Lundgren, E.; Köhler, L.; Kresse, G.; Schmid, M.; Varga, P.; Yuhura, J.; Torrelles, X.; Quirós, C.; Andersen, J. N. Self-Limited Growth of a Thin Oxide Layer on Rh(111). *Phys. Rev. Lett.* **2004**, *92*, 126102–1 – 126102–4.

(81) Lundgren, E.; Gustafson, J.; Mikkelsen, A.; Andersen, J. N.; Stierle, A.; Dosch, H.; Todovora, M.; Rogal, J.; Reuter, K.; Scheffler, M. Kinetic Hindrance During the Initial Oxidation of Pd(100) at Ambient Pressures. *Phys. Rev. Lett.* **2004**, *92*, 046101–1 – 046101–4.

(82) Seriani, N.; Jin, Z.; Pompe, W.; Ciacchi, L. C. Density Functional Theory Study of Platinum

Oxides: From Infinite Crystals to Nanoscopic Particles. *Phys. Rev. B.* **2007**, *76*, 155421–1 – 155421–10.

(83) Ono, L. K.; Yuan, B.; Heinrich, H.; Roldán Cuenya, B. Formation and Thermal Stability of Platinum Oxides on Size-Selected Platinum Nanoparticles: Support Effects. *J. Phys. Chem. C* **2010**, *114*, 22119–22133.

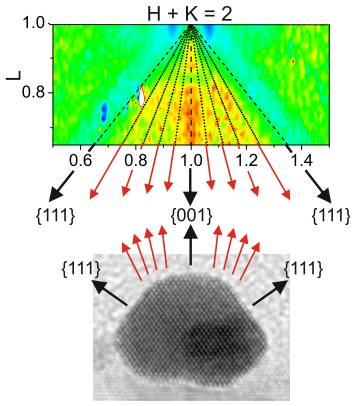

This material is available free of charge via the Internet at `http://pubs.acs.org/`.